Available online at www.sciencedirect.com
ScienceDirect
Journal of Power Sources 178 (2008) 248–257
JOURNAL OF POWER SOURCES
www.elsevier.com/locate/jpowsour

Multi-phase micro-scale flow simulation in the electrodes of a PEM fuel cell by lattice Boltzmann method

J. Park, X. Li *

Department of Mechanical and Mechatronics Engineering, University of Waterloo, 220 University Avenue West, Waterloo, Ontario, Canada N2L 3G1

Received 14 October 2007; received in revised form 30 November 2007; accepted 3 December 2007
Available online 14 December 2007

Abstract

The gas diffusion layer of a polymer electrolyte membrane (PEM) fuel cell is a porous medium generally made of carbon cloth or paper. The gas diffusion layer has been modeled conventionally as a homogeneous porous medium with a constant permeability in the literature of PEM fuel cell. However, in fact, the permeability of such fibrous porous medium is strongly affected by the fiber orientation having non-isotropic permeability. In this work, the lattice Boltzmann (LB) method is applied to the multi-phase flow phenomenon in the inhomogeneous gas diffusion layer of a PEM fuel cell. The inhomogeneous porous structure of the carbon cloth and carbon paper has been modeled as void space and porous area using Stokes/Brinkman formulation and void space and impermeable fiber distributions obtained from various microscopic images. The permeability of the porous medium is calculated and compared to the experimental measurements in literature showing a good agreement. Simulation results for various fiber distributions indicate that the permeability of the medium is strongly influenced by the effect of fiber orientation. Present lattice Boltzmann flow models are applied to the multi-phase flow simulations by incorporating multi-component LB model with inter-particle interaction forces. The model successfully simulates the complicated unsteady behaviors of liquid droplet motion in the porous medium providing a useful tool to investigate the mechanism of liquid water accumulation/removal in a gas diffusion layer of a PEM fuel cell.

Keywords: Lattice Boltzmann simulation; PEM fuel cell; Gas diffusion layer; Permeability; Two-phase flow

1. Introduction

Owing to its high efficiency, zero emission and low operating temperature, polymer electrolyte membrane (PEM) fuel cell has been widely considered as a promising alternative power source for mobile, portable and stationary co-generation. A PEM fuel cell consists of a membrane electrolyte assembly (MEA) sandwiched between two bipolar plates as shown in Fig. 1. The gas diffusion layer (GDL), catalyst layer and polymer electrolyte membrane are referred to as MEA where current is produced. The GDL is a porous medium generally made of carbon cloth or paper and provides essential roles in a PEM fuel cell operation such as electronic conductivity, reactant access to the catalyst layers and product removal from it. The performance of a PEM fuel cell deteriorates due to liquid water accumulated in the GDL and, therefore, optimizing the key parameters of the GDL such as thickness, porosity, permeability and wetting characteristics has been of considerable importance for the PEM fuel cell design, operation and eventual commercialization.

Studies on the GDL have been led mostly by experimental studies [1–5]. The pores can be hydrophobic with optimal value of polytetrafluoroethylene (PTFE) not to be congested with liquid water [1]. Water flow in GDL is experimentally investigated for various thicknesses and pore sizes in Benziger et al. [2]. Paganin et al. [1] observed a performance decrement at higher current densities when the GDL thickness is increased. The thickness of the GDL was optimized by a mathematical modeling in Inoue et al. [3] and by cell performance tests in Lee et al. [4] and Jordan et al. [5], with various GDL parameters such as porosity and thickness. A thin GDL with small porosity results in good electrical conductivity, however efficient mass transport requires large pores, i.e. large porosity. With a small and long serpentine flow channel that can be considered as many parallel channels connected in series, reactants can directly cross to neighboring flow channels due to high pressure gradient and short flow path [6–9]. The amount of cross flow is strongly cor-

* Corresponding author.
E-mail address: x6li@uwaterloo.ca (X. Li).

0378-7753/$ – see front matter © 2007 Elsevier B.V. All rights reserved.
doi:10.1016/j.jpowsour.2007.12.008

Nomenclature

Ca	capillary number
c	δ_x/δ_t
c_s	sound speed
$\mathbf{e}_i$	velocity vector for the lattice Boltzmann model
$f_i(\mathbf{x}, t)$	distribution function
$f_i^{eq}(\boldsymbol{x}, t)$	equilibrium distribution function
$\mathbf{G}$	a potential that couples nearest and next-nearest neighbors.
k	species number
K	permeability of the medium
K_{tow}	tow permeability
$\mathbf{K}_{tow}$	permeability tensor
L	characteristic length
m	molecular weight
N	number of grid points
P	pressure
R	universal gas constant
Re_L	Reynolds number
T	absolute temperature
$\mathbf{u}$	velocity vector
u_x	velocity in x-direction
u_y	velocity in y-direction
V	characteristic velocity
$\mathbf{X}$	position vector

Greek letters

β	a parameter controlling the magnitude of the momentum sink
δ_x	the distance between abutting lattices
δ_t	time step
μ	viscosity of fluid
ν	kinematic viscosity
ρ	density of fluid
σ	species number
τ	relaxation time
ϕ	porosity, N_{void}/N_{total}
Ψ_σ	an arbitrary function of density distribution for species σ
ω_i	weight coefficient for the lattice Boltzmann model

Subscripts

in	inlet
max	maximum value
min	minimum value
out	outlet
void	void region in the GDL
total	the total region in the GDL
x	x-direction
y	y-direction
z	z-direction

related with the thickness and permeability of the GDL in a PEM fuel cell with a serpentine flow channel [6–8]. It was also shown that such cross flow can be effective for the removal of liquid water from the gas diffusion layer [9]. The GDL made of carbon cloth or paper normally has anisotropic permeability for two major orientations: in-plane and through the plane direction. The in-plane permeabilities of various GDLs were measured from the order of 10^{-12} to 10^{-11} m^2 in Feser et al. [10].

A conventional numerical treatment of the GDL in a PEM fuel cell is modeling the entire GDL as a homogeneous porous medium having isotropic or anisotropic permeability [11–13]. The method is numerically efficient since it does not demand a fine grid to capture the microscopic structure of the GDL. However the result of this model is mainly dependant on the given value of permeability which may not be known for the various porous materials of GDLs and it is not proper to utilize the method to investigate the effect of fiber structure and surface condition on the permeability of the medium. Although it may require large computing power, the true geometry of the porous medium can be modeled directly from the microscopic photography of the medium. Joshi et al. [14] applied the lattice Boltzmann (LB) method to a modeling of multi-component gas transport in a solid oxide fuel cell (SOFC). The porous structure of the SOFC is modeled as void space and impermeable solid obstacle from the scanning electron microscope (SEM) image of the porous electrode. The LB model could successfully simulate the diffusive flow in the porous electrode of SOFC without empirical modification of diffusion coefficients using medium porosity and tortuosity [14]. An intermediate scheme to model the flow in a porous electrode may be the application of the Stokes/Brinkman formulations to allow fluid transport through finite-sized porous objects by treating them as an effective medium with a known permeability [15,16]. Spaid and Phelan [15] showed that the effective permeability of the porous medium calculated by LB model well matches an analytical calculation by Phelan and Wise [17]. Park et al. [16] performed 3D LB simulation and observed that the permeability of porous medium is strongly dependant on the fiber tow orientation.

The LB method has been accepted as a new computational tool for a variety of fluid transport phenomena [18]. It was applied to incompressible fluid flows [19,20], transport of passive scalars [21], miscible and immiscible fluids in complex geometries [22] and two-phase flow with phase change [23]. The kinetic nature of the LB method was also shown to be applicable to simulation of chemical reaction in micro- and meso-scopic flow [24] and electrokinetic transport phenomena [25]. In this work, we have modeled the two representative GDL materials, woven carbon cloth and carbon paper, via LB method. The true porous structure of carbon paper was directly taken from microscopic images following Joshi et al. [14]. The permeability has been obtained for the various sample images of carbon papers and compared with the experimental measurements by Feser et al. [10]. We also present an unsteady two-phase LB flow simulation which is applied to the study of liquid water removal from the porous electrode of a PEM fuel cell.

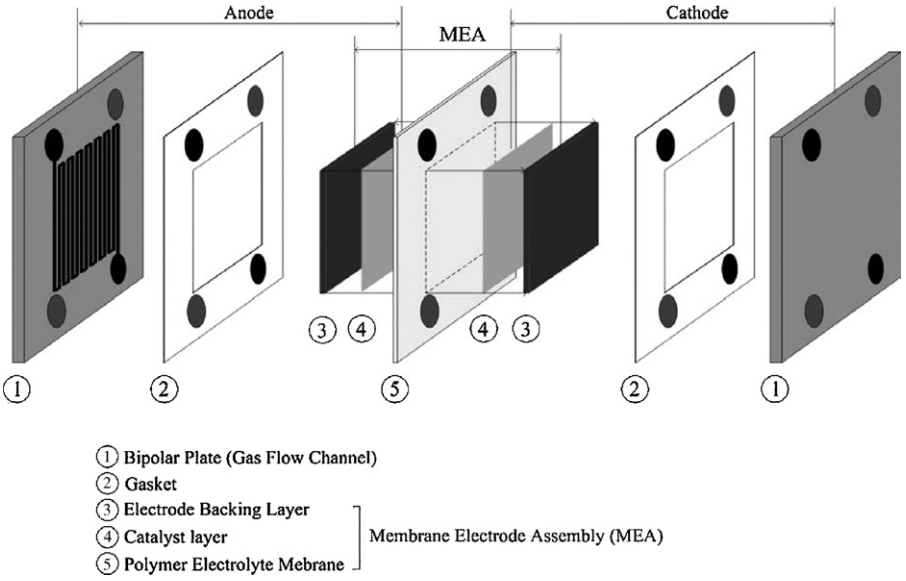

Fig. 1. Schematic of a polymer electrolyte membrane (PEM) fuel cell assembly.

2. Numerical section

2.1. Lattice Boltzmann model

The LB method is based on a finite number of identical particles that go through collision and propagation successively on prefixed paths in space. The following single-component lattice Boltzmann equation describes evolution of the distribution function, $f_i(\mathbf{x}, t)$, with the BGK collision term [26,27]:

$$f_i(\boldsymbol{x} + \boldsymbol{e}_i\delta_t, t + \delta_t) - f_i(\boldsymbol{x}, t) = -\frac{f_i(\boldsymbol{x}, t) - f_i^{\mathrm{eq}}(\boldsymbol{x}, t)}{\tau_v}, \tag{1}$$

where $\mathbf{e}_i$'s are the discrete velocities, δ_i is the time step and τ_v is the relaxation time. f_i^{eq} represents the equilibrium distribution of f_i given as

$$f_i^{\mathrm{eq}}(\rho, \boldsymbol{u}) = \omega_i\rho\left[1 + \frac{\boldsymbol{e}_i\cdot\boldsymbol{u}}{RT} + \frac{(\boldsymbol{e}_i\cdot\boldsymbol{u})^2}{2(RT)^2} - \frac{\boldsymbol{u}\cdot\boldsymbol{u}}{2RT}\right]$$

$$\omega_i = \begin{cases} 4/9, & i = 0 \\ 1/9, & i = 1, 2, 3, 4 \\ 1/36, & i = 5, 6, 7, 8 \end{cases}, \tag{2}$$

where ω_i's are the associated weight coefficients, R is the universal gas constant and T is the absolute temperature. In Fig. 2 the velocity vectors, $\mathbf{e}_i$, for the two-dimensional 9-speed model (D2Q9) are shown to be

$$\boldsymbol{e}_i = \begin{bmatrix} (0,0), & \text{for} \quad i = 0 \\ c\left(\cos\dfrac{i-1}{2}\pi,\ \sin\dfrac{i-1}{2}\pi\right), & \text{for} \quad i = 1, 2, 3, 4 \\ \sqrt{2}c\left(\cos\dfrac{i-4-1/2}{2}\pi,\ \sin\dfrac{i-4-1/2}{2}\pi\right), & \text{for} \quad i = 5, 6, 7, 8 \end{bmatrix}, \tag{3}$$

where $c = \delta_x/\delta_t$, and δ_x is the distance between lattice points. The speed of the sound is $c/\sqrt{3}$ in the phase space and accordingly we have $RT = c^2/3$ and the fluid pressure is given in terms of the fluid density as $p = \rho/3$. The macroscopic number density, $\rho(\mathbf{x}, t)$, and the velocity, $\mathbf{u}(\mathbf{x}, t)$, of the fluid are obtained as

$$\rho = \sum_{i=0}^{8} m f_i, \tag{4}$$

$$\rho\boldsymbol{u} = \sum_{i=0}^{8} m f_i \boldsymbol{e}_i, \tag{5}$$

where the molecular weight, m, is assumed to be unity in the present work. The kinematic viscosity is related to the relaxation time as

$$\nu = \frac{(2\tau_v - 1)}{6}\frac{\delta_x^2}{\delta_t}. \tag{6}$$

Through Chapman–Enskog expansion, Eqs. (1) and (2) lead to the continuity and the Navier–Stokes equations near the

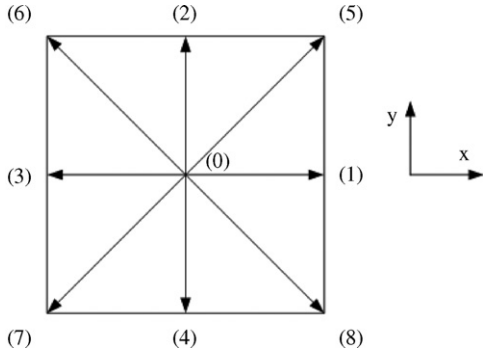

Fig. 2. Lattice structure of the 2D (D2Q9) lattice Boltzmann model.

incompressible limit [28]:

$$\frac{\partial \rho}{\partial t} + \nabla \cdot (\rho \boldsymbol{u}) = 0, \tag{7}$$

$$\rho \left[\frac{\partial \boldsymbol{u}}{\partial t} + (\boldsymbol{u}.\nabla)\boldsymbol{u} \right] = -\nabla p + \nabla \cdot [\rho\nu(\nabla \boldsymbol{u} + \nabla \boldsymbol{u}^{\mathrm{T}})]. \tag{8}$$

2.2. Multi-component lattice Boltzmann model

The multi-component LB model with inter-particle interaction [20,29] was developed for simulation of multi-phase flows and phase transitions. When the interaction is weak this model can be applied to simulate diffusion due to various driving mechanisms [20,25,29]. If any external force is applied to component k the momentum should be incremented correspondingly. In LB method, this is simply achieved by replacing $\mathbf{u}$ in each density equilibrium function with $\mathbf{u}' + \tau_\sigma \mathbf{F}_\sigma/\rho_\sigma$. General form of interaction force between different components at site $\mathbf{x}$ is

$$F_{s\sigma} = -\psi_\sigma(\mathbf{x}) \sum_i \sum_{\bar{\sigma}} G_{\sigma\bar{\sigma}}(\boldsymbol{x}, \boldsymbol{x} + \boldsymbol{e}_i)\psi_{\bar{\sigma}}(\boldsymbol{x} + \boldsymbol{e}_i)\boldsymbol{e}_i, \tag{9}$$

where Ψ_σ is an arbitrary function of density distribution, taken as f_i^σ in this study. In the D2Q9 lattice model, $\boldsymbol{G}_{\sigma\bar{\sigma}}$ describes a potential that couples nearest and next-nearest neighbors as follows:

$$\boldsymbol{G}_{\sigma\bar{\sigma}}(\boldsymbol{x}, \boldsymbol{x}') = \begin{cases} g_{\sigma\bar{\sigma}}, & |\boldsymbol{x} - \boldsymbol{x}'| = 1 \\ g_{\sigma\bar{\sigma}}/4, & |\boldsymbol{x} - \boldsymbol{x}'| = \sqrt{2} \\ 0, & \text{otherwise} \end{cases}. \tag{10}$$

Here $g_{\sigma\bar{\sigma}}$ is the strength of the inter-particle potential between component σ and $\bar{\sigma}$. The wall is regarded as a phase with a constant number density. The interactive force between the fluid and wall is described as

$$\boldsymbol{F}_{\mathrm{w}\sigma} = -\psi_\sigma(\mathbf{x}) \sum_i \boldsymbol{G}_{\sigma\mathrm{w}}(\boldsymbol{x}, \boldsymbol{x} + \boldsymbol{e}_i) f_{\mathrm{w}}(\boldsymbol{x} + \boldsymbol{e}_i)\boldsymbol{e}_i, \tag{11}$$

where the f_{w} is the number density of the wall, which is constant at the wall and zero elsewhere. $\boldsymbol{G}_{\sigma\mathrm{w}}$ is similar with $\boldsymbol{G}_{\sigma\bar{\sigma}}$ while positive for a nonwetting and negative for wetting fluid. Note that introduction of fluid–solid interaction has no effect on the macroscopic equations since it only exists at the solid/fluid interface. The Chapman–Enskog expansion procedure can be carried out to obtain the following continuity and momentum equations for the fluid mixture as a single fluid.

$$\frac{\partial \rho}{\partial t} + \nabla \cdot (\rho \boldsymbol{u}) = 0 \tag{12}$$

$$\rho \left[\frac{\partial \boldsymbol{u}}{\partial t} + (\boldsymbol{u} \cdot \nabla)\boldsymbol{u} \right] = -\nabla p + \nabla \cdot [\rho\nu(\nabla \boldsymbol{u} + \nabla \boldsymbol{u}^{\mathrm{T}})], \tag{13}$$

where $\rho = \sum_\sigma \rho_\sigma$ is the total density of the fluid mixture, and the whole fluid velocity $\mathbf{u}$ is defined as

$$\rho \boldsymbol{u} = \sum\nolimits_\sigma \rho_\sigma \boldsymbol{u}_\sigma + \frac{1}{2}\boldsymbol{F}_\sigma. \tag{14}$$

2.3. Boundary conditions

The practical flow situation in a PEM fuel cell employs some forms of flow regulations at the inlet, outlet and other boundaries. Common types of regulations are constant-velocity, constant pressure and no-slip wall. For the D2Q9 model, we utilized the bounce-back rule to determine unknown part of particle distribution functions [31]. As an example, it is considered that the boundary is aligned with the x-direction with f_4, f_7, f_8 pointing into the wall as shown in Fig. 2. After streaming, $f_0, f_1, f_3, f_4, f_7, f_8$ are known. Supposing that u_x and u_y are specified on the boundary Eqs. (4) and (5) are used to determine f_2, f_5, f_6 and ρ as follows

$$f_2 + f_5 + f_6 = \rho - (f_0 + f_1 + f_3 + f_4 + f_7 + f_8), \tag{15}$$

$$f_5 - f_6 = \rho u_x - (f_1 - f_3 - f_7 + f_8), \tag{16}$$

$$f_2 + f_5 + f_6 = \rho u_y + (f_4 + f_7 + f_8), \tag{17}$$

$$\rho = \frac{1}{1 - u_y}[f_0 + f_1 + f_3 + 2(f_4 + f_7 + f_8)]. \tag{18}$$

To close the system of equations above, we assume the bounce-back rule for the non-equilibrium part of the particle distribution normal to the boundary (in this case, $f_2 - f_2^{(\mathrm{eq})} = f_4 - f_4^{(\mathrm{eq})}$). With f_2 known f_5 and f_6 can be found, thus

$$f_2 = f_4 + \frac{2}{3}\rho u_y, \tag{19}$$

$$f_5 = f_7 - \frac{1}{2}(f_1 - f_3) + \frac{1}{2}\rho u_x + \frac{1}{6}\rho u_y, \tag{20}$$

$$f_6 = f_8 - \frac{1}{2}(f_1 - f_3) - \frac{1}{2}\rho u_x + \frac{1}{6}\rho u_y. \tag{21}$$

The collision is also applied to the boundary nodes. No slip wall can be achieved applying velocities on the wall equals zero ($u_x = u_y = 0$) on the boundary. Similarly, when the density (pressure) is known on the boundary and the velocity is assumed to be normal to the boundary ($u_x = 0$), the unknowns (u_y, f_5, f_6) can be determined from Eqs. (17)–(20) as

$$u_y = 1 - \frac{f_0 + f_1 + f_3 + 2(f_4 + f_7 + f_8)}{\rho_{\mathrm{in}}}, \tag{22}$$

$$f_2 = f_4 + \frac{2}{3}\rho u_y, \tag{23}$$

$$f_5 = f_7 - \frac{1}{2}(f_1 - f_3) + \frac{1}{6}\rho u_y \tag{24}$$

$$f_6 = f_8 - \frac{1}{2}(f_1 - f_3) + \frac{1}{6}\rho u_y. \tag{25}$$

The entire operation is executed after streaming and before collision. Obstacles (carbon fiber) within the numerical domain are also treated like impermeable walls with no mass flux in a direction normal to their surface. The tangential velocity of all species at surface of the solid obstacles is assumed to be zero [14,31].

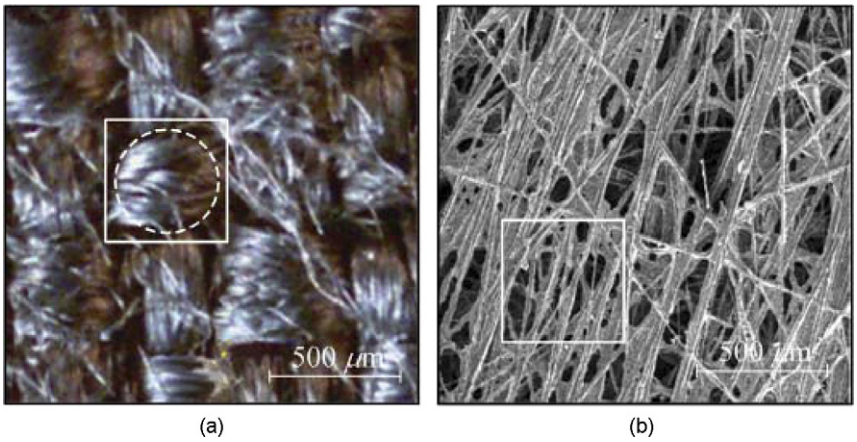

Fig. 3. Microscopic pictures of the carbon gas diffusion media: (a) carbon cloth (a white square represents the computational domain and a white dotted circle the region of tow) and (b) carbon paper (a white square represents the computational domain).

2.4. LB model for the Stokes/Brinkman formulation in a porous medium

Since the LB Stokes/Brinkman formulation is well explained in Spaid and Phelan [15] and Park et al. [16], here, the formulation is briefly introduced for further extension to multi-component LB model. Fluid flow in the open regions is governed by the Stokes equation given by

$$\mu\nabla^2\boldsymbol{u} = \nabla P, \tag{26}$$

where μ is viscosity, $\mathbf{u}$ is velocity vector and P is pressure. Inside the porous tows, the flow is modeled by the Brinkman equation:

$$\mu\nabla^2\langle\boldsymbol{u}\rangle - \frac{\mu}{\boldsymbol{K}_{\text{tow}}}\cdot\langle\boldsymbol{u}\rangle = \nabla\langle P\rangle, \tag{27}$$

where $\mathbf{K}_{\text{tow}}$ is the permeability tensor for the fiber bundles. To recover the Brinkman equation using a LB method, it is necessary to modify the standard equilibrium distribution function to reduce the magnitude of the momentum, leaving the direction of momentum unchanged. This can be achieved by altering the velocity $\mathbf{u}(\mathbf{x}, t)$ in the equilibrium distribution function by incorporating a forcing term given by

$$\boldsymbol{U} = \boldsymbol{u}(\boldsymbol{x}, t) + s(\boldsymbol{x})\frac{\tau\boldsymbol{F}(\boldsymbol{x}, t)}{\rho(\boldsymbol{x}, t)}, \tag{28}$$

where $\mathbf{U}$ replaces $\mathbf{u}$ in Eq. (5) for the equilibrium distribution function, and the variable $s(\mathbf{x}, t)$ is either 0 or 1 depending on whether a lattice site is located in a void or porous region, respectively. The porous region indicates the fibrous area with flow resistance caused by the friction on the fiber surface while the void region indicates the empty space between fiber bundles with no direct effect of friction as shown in Figs. 3(a) and 4(a). The form of the forcing term $\mathbf{F}(\mathbf{x}, t)$ which is needed to recover the Brinkman equation is given by

$$\boldsymbol{F}(\boldsymbol{x}, t) = -\beta\rho(\boldsymbol{x}, t)\boldsymbol{u}(x, t), \tag{29}$$

where β is a parameter controlling the magnitude of the momentum sink. From Eqs. (28) and (29) the equilibrium velocity in a Brinkman site ($s(\mathbf{x}, t) = 1.0$) is defined as

$$\boldsymbol{U} = \boldsymbol{u}(\boldsymbol{x}, t)(1 - \beta\tau). \tag{30}$$

Then, the LB equation in a Brinkman site is given for the steady state as

$$v\nabla^2\boldsymbol{u} - \beta\boldsymbol{u} = \frac{1}{\rho}\nabla P. \tag{31}$$

Eq. (31) reproduces the Brinkman equation if $\beta = \nu/\mathbf{K}_{\text{tow}}$ in which both the kinematic viscosity and the tow permeability are expressed in lattice units [20]. The validity of LB

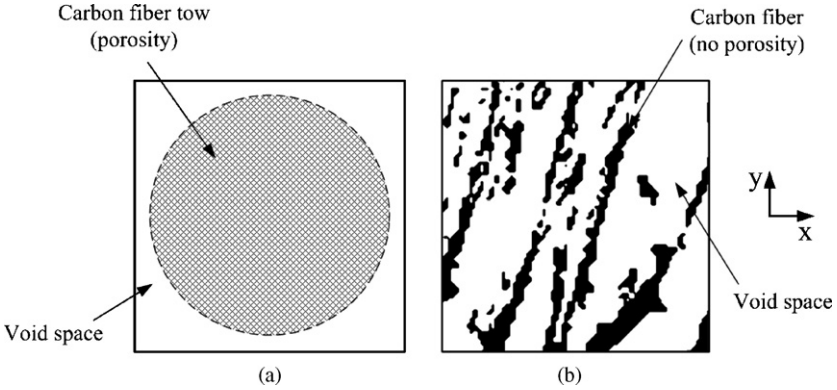

Fig. 4. Lattice Boltzmann models for gas diffusion media: (a) 2D porous model for carbon cloth medium and (b) 2D micro-obstacle model for carbon paper (Case A).

Stokes/Brinkman modeling was verified by comparing the LB simulation results with analytical and experimental measurements in a previous work [16].

3. Results and discussion

The GDL of a PEM fuel cell has been numerically modeled using LB method via two different LB formulations. The woven carbon cloth is modeled as void space and porous area which has certain permeability by the LB Stokes/Brinkman equation [15,16] while randomly distributed fibrous porous structure of the carbon paper is modeled based on the actual microscopic images using the LB solid obstacle modeling. In Section 3.1, the permeability of the modeled medium is compared with experimental measurements in literature [10]. The effect of fiber orientation on the permeability of the porous medium has been investigated within a typical range of porosity. In the following section, the two porous LB flow models are extended to unsteady multi-phase LB simulations in the porous medium. The LB model simulates unsteady motion of a liquid droplet and its breaking up during its passage through a complicated porous medium being driven by ambient fluid convection.

3.1. LB models for the gaseous reactant flow in an inhomogeneous porous medium

Fig. 3(a) and (b) presents the microscopic pictures of the woven carbon cloth and carbon paper, respectively, which are the most common materials for the gas diffusion layers in PEM fuel cells. The porous structure of the carbon cloth consists of carbon fiber tows, the bundles of carbon fiber, and void spaces among tows. The combinational effect of the void space and tow permeability results in the effective permeability of the porous medium. Since the fiber tow has much finer substructures inside compared to its characteristic length scale (i.e. the diameter of the fiber tow) it would be numerically efficient to model the fiber tow as a uniform porous area with certain permeability neglecting its substructure. In Fig. 4(a), the carbon cloth is modeled as consisting of void space and fiber tow area which has certain permeability and the LB Stokes/Brinkman formulation, Eqs. (1)–(5) with extra forcing terms (28)–(30) in porous area, are solved for a transverse flow over 2D porous circle [15,16]. The size of physical domain is 400 μm × 400 μm as shown in Fig. 4(a) and 50 × 50 grid points are given for the numerical domain to model this geometry. The side boundaries are assumed to be periodic based on the fact that the entire medium has the reciprocating pattern of the fiber tow and void space in the plane directions. Meanwhile, the porous structure of the carbon paper may be characterized as void space surrounded by randomly distributed carbon fibers with no distinct pattern found in the carbon cloth. The Stokes/Brinkman formulation is not proper to model the detail of such complicated random structure which has a dominant influence on the permeability of the medium. Therefore, in this work, the true porous structure is recovered from the microscopic image of carbon paper using a large number of grid point (150 × 150) in the physical domain of 400 μm × 400 μm as shown in Fig. 4(b). For this, the microscopic image of carbon paper is converted into a binary data (0: void and 1: solid obstacle) by applying a certain value of threshold. The solid obstacle in the numerical domain is an impermeable object with no slip boundary condition on its surface which is the equivalent surface characteristic of the carbon fiber in the physical domain. In this way, the porosity of the medium can be controlled according to the value of the threshold without altering the major fiber distribution and, in the present LB solid obstacle modeling, the porosity, ϕ, is determined as the ratio of the number of void grid points to the number of total grid points in the converted binary data. Sample images were taken at random position of the images to investigate the effect of fiber orientation and porosity on the resultant permeability of the medium. Fig. 5 shows five different sample media of carbon paper which are chosen for the present LB simulation. Medium A–C are characterized as dominant fiber orientations with relatively low porosities, whereas medium D and E are lack of such dominant fiber orientations with relatively higher porosities.

Fig. 6(a) presents the velocity and pressure distributions in the porous medium modeled by Stokes/Brinkman formulation when the tow permeability, K_{tow}, is 10^{-10} m^2. Constant pressure is applied at the bottom and top surfaces to drive the flow motion while the two vertical surfaces are assumed to be periodic. The velocity vectors are normalized by the maximum velocity in the computational domain where the tow area is marked as a dashed circle. It is seen that the magnitude of velocity is substantially smaller inside the tow area than outside the tow area due to the flow resistance caused by the low permeability of the tow. The pressure contours are symmetrical profiles for the upstream and downstream divided by a straight contour that is normal to the mean flow direction (y-direction). Fig. 6(b) shows veloc-

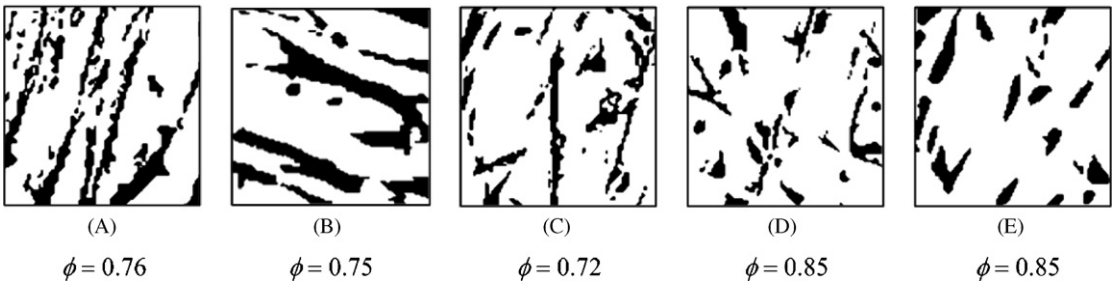

Fig. 5. Numerical models of gas diffusion layer obtained from the various samples of microscopic images (carbon paper); ϕ is the porosity, determined as the ratio of the number of void grid points to the number of total grid points in the converted binary data.

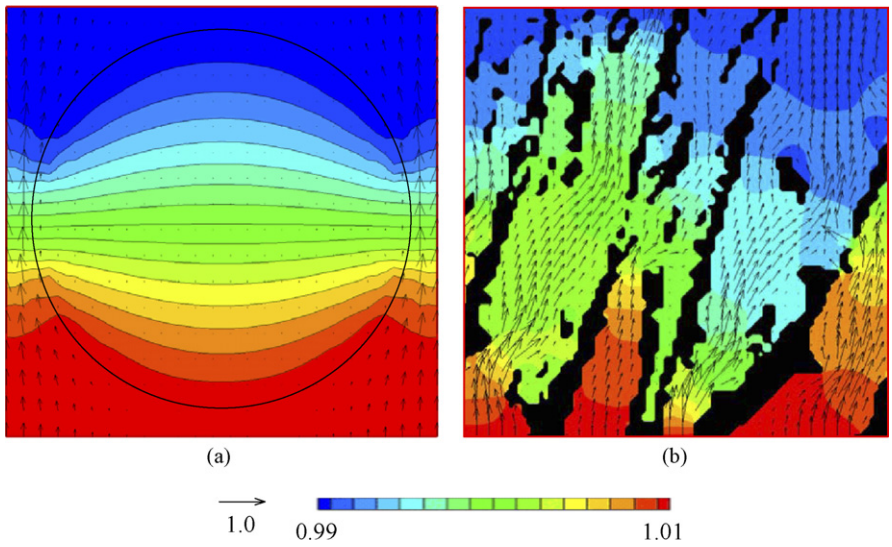

Fig. 6. Lattice Boltzmann simulation results in the gas diffusion media; the vector represents the fluid velocity and the color represents the pressure distribution: (a) porous model for carbon cloth medium, $K_{tow} = 10^{-10}\,m^2$, (b) micro-obstacle model for carbon paper; black colored area represents solid obstacle (Model A), $Re_L = 0.05$ and the pressure and velocity vectors are non-dimensionalized using average pressure and maximum velocity in the domain.

ity and pressure distributions in a porous medium modeled by the LB solid obstacle formulation for the Medium A in Fig. 5. The black colored area represents the impermeable solid obstacles (carbon fibers) and it shows a complicated flow field in the void space among fibers. The flow is squeezed at several narrow paths resulting in a high velocity with a rapid pressure drop. It is also observed that a major flow blockage can be caused by small obstacles regularly distributed in a finite area as seen in the left upper part of Fig. 6(b). On the contrary, the large obstacles parallel with the main flow direction do not necessarily produce large flow resistance. This implies that the permeability of the porous medium is not only dependent on the porosity but also have strong influence from the characteristics of the porous structure.

To investigate the effect of the porous structure such as fiber orientations on the permeability of the porous medium, the flow simulation is performed for the two major perpendicular directions for the various samples of porous medium in Fig. 5. The permeability of the medium is calculated based on the Darcy's law:

$$K = -\frac{\mu \langle \boldsymbol{u} \rangle}{\nabla \langle P \rangle}, \tag{32}$$

where $\langle \mathbf{u} \rangle$ and $\langle P \rangle$ are the average velocity and pressure in the computational domain, respectively. The value of permeability is non-dimensionalized by the length of computational domain, L. In Fig. 7, Medium A and C have higher permeability when the pressure gradient is given for the y-direction due to the fact that main fiber orientations is also parallel with the y-direction as shown in Fig. 5. Similarly, the Medium B has higher permeability for the x-direction with the main fiber direction parallel with x-direction. However such phenomenon is not apparent in case of Medium D and E since the fiber orientation is not obvious for those two samples. The value of permeability varies in a similar range with that of Medium A–C except for the cases of A-x and C-x in Fig. 7 although the porosity of Medium D and E are quite higher than other three media. It seems that the effect of the fiber orientation on the permeability of the medium can be dominant over that of porosity within the given range of porosity.

Fig. 8 compares the permeability of the porous medium obtained by the present LB solid obstacle modeling with the experimental measurements of in-plane permeability for the two different GDLs in Feser et al. [10]. SGL 31BA (SGL Carbon) and TGP-60-H (Toray) are a non-woven carbon fiber and a paper-based carbon fiber, respectively, without micro-porous layers. Both samples contain almost identical porous structures consisting of randomly oriented carbon fibers as the one shown in Fig. 5(b). The porosity of Medium A is modified by adjusting the value of threshold during the image converting process. The LB simulation results present two discrete lines for the different flow directions in Fig. 8 however each line does not show much increment as the porosity of the medium increases from 70 to 80%. This is attributed to the fact that the fibers become thinner but the orientations are not altered as the porosity is increased. It is also observed that the experimental data for various gas diffusion lay-

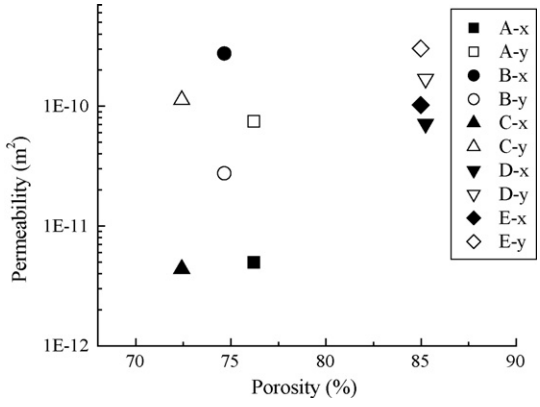

Fig. 7. Permeability of the porous medium for the two main flow directions: x and y in the legend indicate the flow direction considered in the simulation.

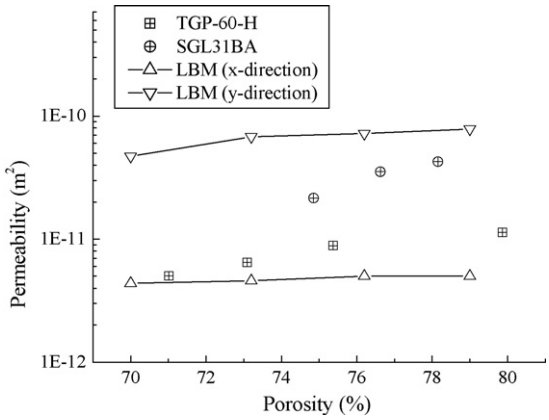

Fig. 8. Comparison of the permeability of the porous medium (Medium A) with experimental measurements of in-plane permeability of various gas diffusion layers (carbon papers) in Feser et al. [10].

ers in Feser et al. [10] fall between these two principal values of permeability. Although it is not so meaningful to compare the LB Stokes/Brinkman modeling and the experimental measurements since the correlation between the porosity and permeability of the fiber tow is not clearly known for the present porous medium, the permeability of the porous medium can be calculated as 2.05×10^{-10} m^2 using LB Stokes/Brinkman model when the diameter, porosity and permeability of the fiber tow are assumed to be 360 μm, 0.65 and 1.23×10^{-10} m^2, respectively, so that the medium has the porosity of 0.77. This value is one order of magnitude larger than the experimental measurements in Fig. 8 and the difference is mainly attributed to neglecting the structural effect in the Stokes/Brinkman model.

3.2. LB multi-phase flow simulation in a porous medium

One of the primary advantages of LB methods for simulating fluid flows as compared to the traditional numerical methods is their ability to robustly model interfaces between two or more fluids in complicated geometries such as porous medium. The mechanism of liquid water accumulation in the GDL is of great interest for PEM fuel cell researchers since the phenomenon is widely accepted as one of the main mechanisms which limit the performance of a PEM fuel cell. In this section, the two flow models in the previous section are extended to multi-phase LB simulations by incorporating the inter-particle interaction model [20,29]. The magnitude of inter-particle force is set through the value of $g_{\sigma\bar{\sigma}}$ in Eq. (10). Then the viscosity of the fluid is given as

$$\nu = \frac{1}{3}\left(\sum_{\sigma}\beta_\sigma \tau_\sigma - \frac{1}{2}\right), \tag{33}$$

where β_σ is the mass density concentration of the kth component and is defined as

$$\beta_\sigma = \frac{\rho_\sigma}{\sum_\sigma \rho_\sigma}. \tag{34}$$

The multi-phase flow in porous medium involves low velocity and dominant effect of capillary forces between fluid/fluid and fluid/surface interfaces. The phenomenon can be characterized by the capillary number which represents the relative effect of viscous forces versus surface tension acting across an interface between a liquid and a gas, or between two immiscible liquids.

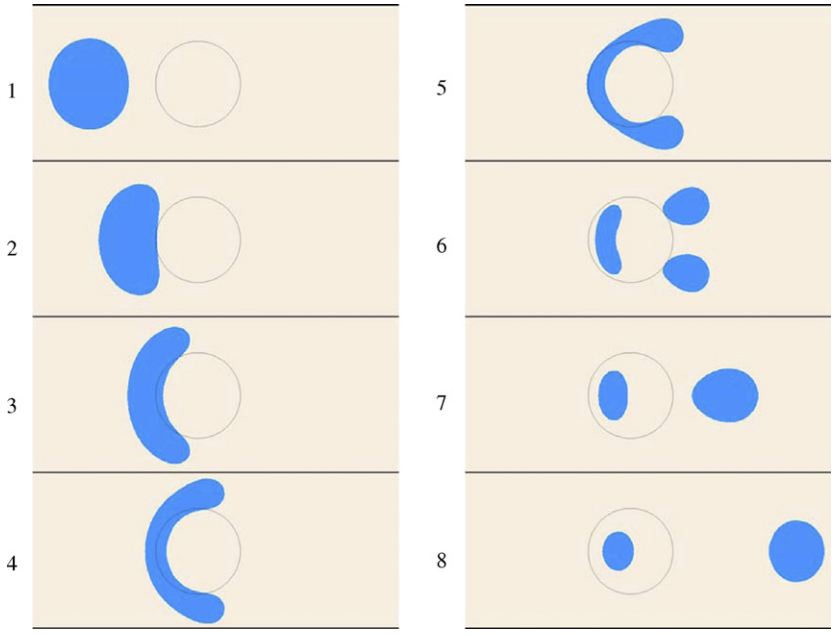

Fig. 9. Unsteady two-phase simulation results using the LB Stokes–Brinkman model incorporated with inter-particle interaction model [29]; blue area is the liquid water and the interior of the dotted circle indicates the porous region representing a fiber tow of the carbon cloth GDL. (1 and 2) Liquid droplet starts to move, driven by the mean flow motion; (3–6) droplet deforms and stretched around the porous region; (7 and 8) detached droplets merge and leave the porous area while a part of liquid water is trapped and remains inside in the porous area. $Re_L = 0.1$, $Ca = 2.3 \times 10^{-5}$ and $K_{tow} = 10^{-9}$ m^2. (For interpretation of the references to color in this artwork, the reader is referred to the web version of the article.)

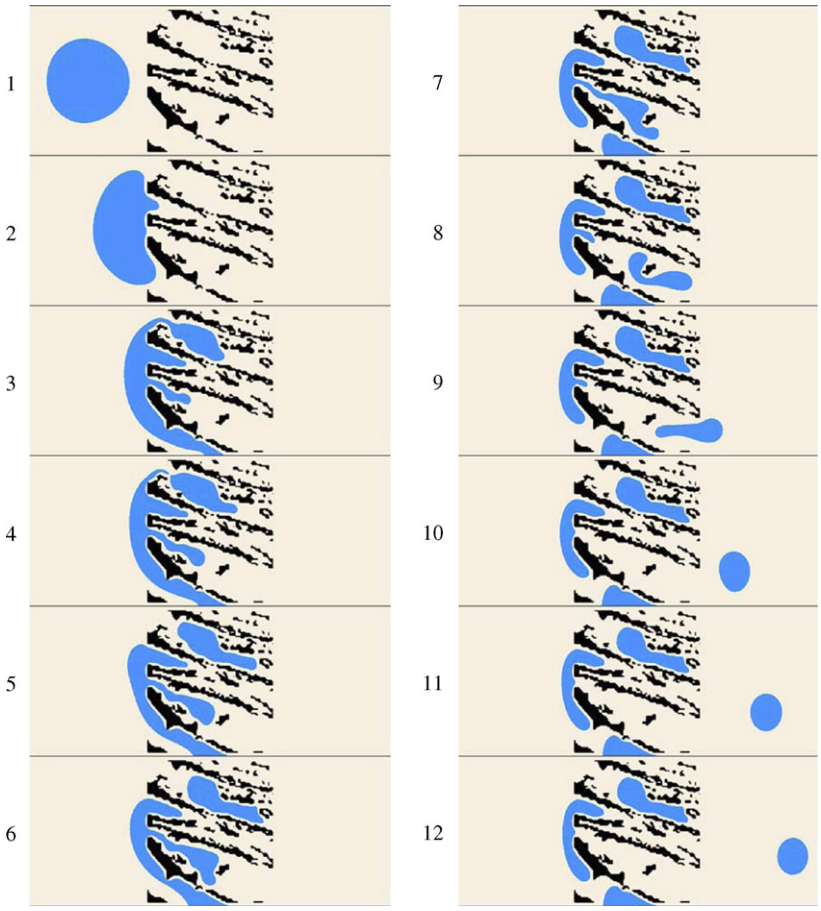

Fig. 10. Unsteady two-phase simulation results using LB binary fluid model simulating two-phase flow through fibrous structure of carbon paper GDL; blue area is the liquid drop and black colored area indicates solid obstacle (carbon fiber). (1 and 2) Liquid droplet starts to move, driven by the mean flow and hit the porous surface; (3–8) droplet deforms and breaks up into smaller ligaments moving into the porous region; (9–12) detached droplets leave the porous area while the major part of liquid water is trapped and remains in the porous area. $Re_L = 0.1$ and $Ca = 2.3 \times 10^{-5}$. (For interpretation of the references to color in this artwork, the reader is referred to the web version of the article.)

It is defined as

$$Ca = \frac{\mu V}{\varepsilon}, \tag{35}$$

where V is a characteristic velocity and ε is the surface or interfacial tension between the two fluid phases. In this work, the surface tension between each fluid is estimated from Laplace's law following Kang et al. [34] and the resultant capillary number, Ca, for this simulation is found to be 2.3×10^{-5} that is within a typical range of Ca for the air/liquid water interface in a porous medium. In case of Stokes/Brinkman model, the velocity of each component is replaced with Eq. (28) in the porous region as a result of drag force. The Reynolds number is defined using the average velocity at the inlet, V, and the thickness of the computational domain, L as

$$Re_L = \frac{\rho V L}{\mu}. \tag{36}$$

Present model consists of two fluids (blue and white), as shown in Fig. 9, which may represent liquid water and gaseous reactant in a PEM fuel cell, respectively. Fig. 9 presents unsteady multi-component LB simulation results based on the Stokes/Brinkman formulation. The relaxation time, τ, is fixed as unity for both components and the density ratio of the blue to white fluid is set to be 2.0. The top and bottom surfaces are assigned to be no slip walls and the constant pressure is given for the white fluid at the inlet (left wall) and outlet (right wall) boundaries to push the blue fluid toward the x-direction. As a result, the blue droplet starts to move, driven by the mean flow motion of the white fluid as shown in Fig. 9(1) and (2). The blue droplet deforms continually and is stretched around the porous region pushed by the white fluid in Fig. 9(3)–(5). In the meanwhile, the stretched part of blue fluid penetrates into the porous region. The blue fluid eventually breaks up into three subparts in Fig. 9(6). The two detached droplets flow around the porous region and then merge together as one larger droplet in Fig. 9(7). This larger droplet continues to move along with the mean flow motion while the smaller one left behind is trapped in the porous area as shown in Fig. 9(8).

Fig. 10 presents another unsteady two-phase simulation of the liquid droplet passing through the complicated porous medium representing carbon paper GDL (Medium A) using LB solid obstacle modeling incorporated with multi-component LB model. The boundary conditions are the same as those of previ-

ous two-phase LB simulation. The surface condition of fibrous porous structure is controlled by the value of $\mathbf{G}_{\sigma w}$ in Eq. (12), and is given as 0.1 to generate wetting condition for the present case. It should be noted that the mixed wetting surface condition [35–37] in a practical GDL may be modeled by alternating the value of $\mathbf{G}_{\sigma w}$ for selected surfaces or regions in the domain. In Fig. 10(1) and (2), it is seen that the large blue droplet driven by the mean flow motion hits the porous surface. As the droplet is pushed by the white fluid it starts to deform and is squeezed into the void space in the porous medium in Fig. 10(3) and (4) and, later a chunk of the blue fluid is detached and accumulated in the upper part of porous medium in Fig. 10(5). The major part of blue fluid breaks up into three subparts in Fig. 10(6)–(8) and each detached sub-droplets reshape its form due to the surface tension of the fluid. In Fig. 10(9)–(12), the detached droplets leave the porous area while other three subparts of liquid water are trapped and remain in the void space of the medium. Present LB model predicts well the unsteady liquid water accumulation/removal process under a strong ambient convective flow in a porous medium. The model would be useful tool to investigate the liquid water removal from a gas diffusion layer under land area utilizing cross-leakage flow [9]. Although not shown here, higher pressure and hydrophobic surface condition resulted in more efficient liquid water removal from the porous medium. While, for strict comparison with experimental observations, it may require higher density ratio between each fluid which is the case of the interface between air and liquid water. The density ratio of the present multi-component model is confined to O(1) due to the stability issues [20,29]. There exist a few recently developed LB models [38,39] available for the multi-phase flow simulation in a higher density ratio up to 1000 although their stability is not yet proven in a complicated geometry.

4. Concluding remarks

In this work, lattice Boltzmann method has been applied to model the multi-phase micro-scale flow through the gas diffusion layers in a PEM fuel cell that are made of carbon cloth and carbon paper, respectively. The woven carbon cloth is modeled as void space and porous area with certain permeability while randomly distributed fibrous structure of the carbon paper is directly modeled based on the microscopic images of the structure and it is treated as impermeable obstacles. The model predictions match well with the experimental measurements of permeability in literature. The effect of fiber orientation on the permeability of the medium is investigated on the basis of various sample images of carbon paper. The permeability varies considerably according to the flow direction indicating that the effect of fiber orientation is critical to the directional dependence of the permeability of inhomogeneous porous medium. Multi-phase lattice Boltzmann porous model has been developed on the basis of the two LB flow models by incorporating multi-component LB model with inter-particle forces. The model successfully simulates the unsteady characteristic behaviors of liquid droplet motion in the porous medium providing a useful tool to investigate the mechanism of liquid water accumulation/removal in the porous electrode of a PEM fuel cell.

Acknowledgment

This work was supported by AUTO21, the Network of Centers of Excellence, Canada.

References

[1] V.A. Paganin, E.A. Ticcianelli, E.R. Gonzalez, J. Appl. Electrochem. 26 (3) (1996) 297.
[2] J. Benziger, J. Nehlsen, D. Blackwell, T. Brennan, J. Itescu, J. Membr. Sci. 261 (2005) 98–106.
[3] G. Inoue, Y. Matsukuma, M. Minemoto, J. Power Sources 154 (2006) 8–17.
[4] H. Lee, J. Park, D. Kim, T. Lee, J. Power Sources 131 (2004) 200–206.
[5] L. Jordan, A. Shukla, T. Beehrsing, N. Avery, B. Muddle, M. Forsyth, J. Power Sources (2000) 250–254.
[6] J. Park, X. Li, J. Power Sources 163 (2007) 853–863.
[7] G. Inoue, Y. Matsukuma, M. Minemoto, J. Power Sources 157 (2006) 136–152.
[8] T. Kanezaki, X. Li, J.J. Baschuk, J. Power Sources 162 (2006) 415–425.
[9] J. Park, X. Li, D. Tran, T. Abdel-Baset, D.S. Hussey, D.L. Jacobson, M. Arif, Int. J. Hydrogen Energ., in press.
[10] J.P. Feser, A.K. Prasad, S.G. Advani, J. Power Sources 162 (2006) 1226.
[11] S. Dutta, S. Shimpalee, J.W. Van Zee, Int. J. Heat Mass Transf. 44 (2001) 2029.
[12] J.G. Pharoah, J. Power Sources 144 (2005) 77.
[13] J. Park, X. Li, J. Power Sources 163 (2007) 853.
[14] A.S. Joshi, K.N. Gre, A.A. Peracchio, W.K.S. Chiu, J. Power Sources 164 (2007) 631.
[15] M. Spaid, F.R. Phelan Jr., Phys. Fluids 9 (1997) 2468.
[16] J. Park, M. Matsubara, X. Li, J. Power Sources 173 (2007) 404–414.
[17] F.R. Phelan Jr., G. Wise, Composites 27A (1995) 25.
[18] X. He, L. Luo, J. Stat. Phys. 88 (1997) 927.
[19] A. Cali, S. Succi, A. Cancelliere, R. Benzi, M. Gramignani, Phys. Rev. A 45 (1992) 5771.
[20] X.W. Shan, H.D. Chen, Phys. Rev. E 47 (1993) 1815.
[21] B.J. Palmer, D.R. Rector, Phys. Rev. E 61 (2000) 5295.
[22] S.P. Dawson, S. Chen, G.D. Doolen, J. Chem. Phys. 98 (1993) 1514.
[23] X. He, N. Li, Comput. Phys. Commun. 129 (2000) 158.
[24] B. Li, D.Y. Kwok, Int. Heat Mass Transf. 46 (2003) 4235.
[25] J. Park, K.Y. Huh, X. Li, J. Electroanal. Chem. 591 (2006) 141.
[26] P.L. Bhatnagar, E.P. Gross, M. Krook, Phys. Rev. 94 (1954) 511.
[27] X. He, L. Luo, Phys. Rev. E 56 (1997) 6811.
[28] H. Chen, S. Chen, W.H. Matthaeus, Phys. Rev. A 45 (1992) R5339.
[29] X. Shan, H. Chen, Phys. Rev. E 49 (1994) 2941.
[31] Q. Zou, X. He, Phys. Fluids 9 (1997) 1591–1598.
[34] Q. Kang, D. Zhang, S. Chen, Phys. Fluids 14 (2002) 3203.
[35] E.C. Kumbur, K.V. Sharp, M.M. Mench, J. Power Sources 168 (2007) 356.
[36] N. Djilali, D. Lu, Int. J. Therm. Sci. 41 (2002) 29.
[37] Q. Ye, T.V. Nguyen, J. Electrochem. Soc. 154 (2007) B1242.
[38] T. Inamuro, T. Ogata, S. Tajima, N. Konishi, J. Comput. Phys. 198 (2004) 628.
[39] T. Lee, C. Lin, J. Comput. Phys. 206 (2005) 16.